

Received 24 March 2023; accepted 25 March 2023. Date of publication 30 March 2023; date of current version 6 December 2023.
The review of this article was arranged by Editor A. Escobosa.

Digital Object Identifier 10.1109/JEDS.2023.3263278

Device Physics, Modeling and Simulation of Organic Electrochemical Transistors

MALTE KOCH¹, HSIN TSENG^{2,3}, ANTON WEISSBACH^{2,3}, BENJAMIN INIGUEZ^{ID 4} (Fellow, IEEE), KARL LEO^{2,3},
ALEXANDER KLOES^{ID 1} (Senior Member, IEEE), HANS KLEEMANN^{2,3}, AND GHADER DARBANDY^{ID 1}

¹ NanoP, TH Mittelhessen University of Applied Sciences, 35390 Giessen, Germany
² Dresden Integrated Center for Applied Physics and Photonic Materials, Technische Universität Dresden, 01062 Dresden, Germany

³ Institute for Applied Physics, Technische Universität Dresden, 01062 Dresden, Germany

⁴ Department of Electronic Engineering, Universitat Rovira i Virgili, 43007 Tarragona, Spain

CORRESPONDING AUTHOR: G. DARBANDY (e-mail: ghader.darbandy@ei.thm.de)

This work was supported in part by the German Research Foundation (DFG) under Grant DA 2578/2-1, and in part by the Bundesministerium für Bildung und Forschung (BMBF) through BAYOEN under Grant 01IS21089.

(Malte Koch and Hsin Tseng contributed equally to this work.)

ABSTRACT In this work, we investigate organic electrochemical transistors (OEETs) as a novel artificial electronic device for the realization of synaptic behavior, bioelectronics, and a variety of applications. A numerical method considering the Poisson-Boltzmann statistics is introduced to reproduce associated charge densities, electrostatics and switching properties of OEETs. We shed light on the working principle of OEETs by taking into account the ionic charge distribution in the electrolyte and incomplete ionization of the organic semiconductor describing the underlying electrochemical redox reaction. This enables analyzing the OEETs electrical performance as well as a simplified chemical properties via an electrical double layer, doping and de-doping of the OMIEC layer. We have fabricated, characterized, simulated and analyzed OEETs based on PEDOT:PSS, and we show that the proposed model reveals important properties of the device's working mechanism. The model shows a good agreement with the experimental data of the fabricated devices.

INDEX TERMS OEETs, synaptic devices, electrical double layer, modeling, simulation.

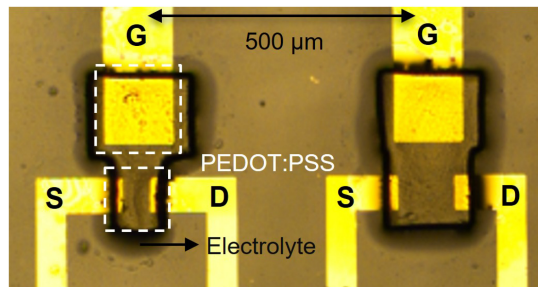
I. INTRODUCTION

Artificial synapses have attracted a lot of interest in recent years to develop neuromorphic architectures and artificial intelligence. They perform signal processing and storage between neurons thus enabling emerging brain-inspired neural networks [1], [2]. Many chemical and biological systems, like a human neuron, do operate mainly on ionic movement [3], [4], which renders OEETs attractive for brain-inspired networks as they operate based on the same principle.

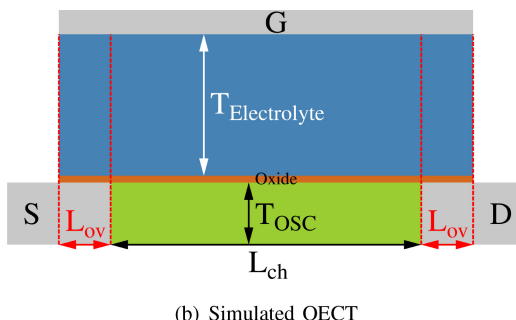
Mobile ions in the electrolyte and the polymeric mixed ionic-electronic conductor (OMIEC) are the key elements for the OEETs and determine the synaptic properties of the devices [5], [6], [7]. The electrochemical interaction between ions and the OMIECs leads to a performance of OEETs with a low gate leakage current, low voltage operation,

high transconductance and exhibit pronounced and reproducible hysteresis in the transfer characteristics [8], [9]. Besides these properties, OMIECs show excellent mechanical properties and offer cost-efficient production, e.g., via low-temperature printing processes [10], [11]. As solid-state electrolyte technology advances [9], [12], [13], OEETs have enormous potential to be integrated into wearable or even implantable electronic systems with intelligent function. Furthermore, the simple manufacturing and good yield of OEETs promise a good scaling solution [14]. The synaptic performance of OEETs are due to the electrochemical gate operation principle rather than electrostatic in their field-effect counterpart [15], [16].

In this work, the fabricated solid-state OEETs with PEDOT:PSS as a channel and their measurements are presented. PEDOT:PSS has been chosen because it is the



(a) Fabricated OECT with solid electrolyte



(b) Simulated OECT

FIGURE 1. (a) Optical microscopic images of a fabricated and (b) schematic cross-section of the simulated OECT, where the device dimensions are given in Table 1.

benchmark material for OECTs and have been widely investigated. The patterned solid electrolyte reduces undesired gate leakage current and confines the volume of electrolyte for each measurements. We have reported a simple method to represent charge distributions and electrolyte behavior in the OECTs [17]. Incomplete ionization for selected species has been considered with an ionization probability model based on activation energy. This model enables the quantitative description of the electric double layer, doping, de-doping of the OMIEC and numerical simulation of OECTs. The simulation results show a good agreement with experimental measurements thus confirming the validity of the presented method and models.

II. DEVICE FABRICATION

The fabricated OECTs consist of metallic source, drain, and gate (gold) electrodes, PEDOT:PSS as a channel material and a solid-state electrolyte between the channel and gate electrode. The gate electrode is also covered with PEDOT:PSS to increase the gate electrode capacitance. This ensures that the gate voltage mainly drops over the channel/interface thus a higher surface potential allows a better carrier modulation inside OMIEC. The microscopic image of the fabricated OECT is shown in Fig. 1(a) and the details of the fabricated OECTs can be found in [9], [14]. Fig. 1(b) shows the simplified schematic cross-section of the simulated device considering a thin layer of oxide between the electrolyte layer and OMIEC. The device dimensions are given in Table 1.

The metallic electrodes were structured on a glass substrate with 50nm Au and 3nm Cr by photolithography.

TABLE 1. OECT dimensions.

| Parameter | Description | Value |
|-------------|-----------------------------|-------------------|
| L_{Ch} | Channel length | 50 μm |
| W_{Ch} | Channel width | 150 μm |
| L_{SD} | Source and Drain length | 15 μm |
| L_{Ov} | Source/Drain - Gate Overlap | 5 μm |
| T_{Elec} | Electrolyte thickness | 3 μm |
| T_{OMIEC} | OMIEC thickness | 100 nm |
| T_{Ox} | Oxide thickness | 1 nm |

PEDOT:PSS films were spin-coated at 3000 rpm resulting in a thickness of 100 nm and structured by fluorine-based photolithography [18] and dry-etching using oxygen plasma [19]. PEDOT:PSS solutions contains 5 v/v% of ethylene glycol and 95 v/v% of PEDOT:PSS (Hearaeus Clevios PH 1000). The solid electrolyte precursor solution was inkjet printed on top of the active area followed by 2 min UV cross-linking. This precursor solution contains 1 mL deionized water, 750 mg N-isopropylacrylamide, 20 mg N,N'-methylenebisacrylamide, 200 mg 2-hydroxy-4'-(2-hydroxyethoxy)-2-methylpropionophenone, and 1.5 mL 1-ethyl-3-methylimidazolium ethyl sulfate. The OECTs were then encapsulated with glass in a glovebox for further and future measurements and characterizations.

A thin layer of oxide between electrolyte and semiconductor has been considered in the simulation to form a double-layer capacitor where the semiconductor is impermeable to ions of the electrolyte. The oxide layer should be considered in a way that the impact of the oxide capacitance can be negligible compared to the capacitance of the electrical double layer. Therefore, the capacitance of the thin layer of Helmholtz plane will be dominant and determines the total capacitance, surface potential and current of the devices. This configuration leads to a very thin layer ($\sim 1 \text{ nm}$ [20]) of ions at the electrolyte-OMIEC interface. Therefore, resulting in a high capacitance that determines the drain current of the transistor independent of electrolyte thickness [21].

III. METHODS AND MODELS

We propose a method to simulate the distribution of ionic charges and correlated ion movement inside an electrolyte solution with the applied biases. An applied gate bias V_{GS} leads to separation and migration of ions in the electrolyte. Assuming an impermeable character of the semiconductor, an electrical double-layer (EDL) can be formed that causes an accumulation of ions at the electrolyte-semiconductor interface.

However, for OMIEC, ions are injected into the OMIECs, which leads to chemical doping/de-doping, volumetric capacitance and a higher conductivity. Here, the origin of the mobile charges comes from the fully oxidized state of the PEDOT^+ . In a device with a permeable junction between electrolyte and OMIEC, a high gate voltage will drive cations into the OMIEC, reducing the polymer to PEDOT^0 and therefore inhibiting the mobile charge. The incomplete ionization model applicable to the specified species has been considered with an ionization probability model based on

activation energy. This model resembles the ionic charge injection and transfer into the OMIEC, thus mimics reduction state and enables electrochemical doping and de-doping. Therefore, a combination of an electrolyte solution and incomplete ionization models enable to simulate and analyze an OMIEC/OECT performance and working principles.

A. ELECTROLYTE MODEL

An electrolyte is defined as an aqueous solution, usually in liquid form [22]. The pH-value is the negative logarithm of the hydrogen ion activity $[H^+]$ in mol per liter of pure water. The pOH, on the other hand, measures the activity of the hydroxide ion activity $[OH^-]$

$$\begin{cases} pH = -\log_{10}[H^+] \\ pOH = -\log_{10}[OH^-] \end{cases} \quad (1)$$

The total ionic density of an electrolyte has been calculated solely based on the pH-value [17], [23]. But this will underestimate the ionic charge density where other solvents for instance NaCl are supposed to be considered. In such cases there is an additional increase of ionic charge density in an electrolyte without changing its pH-value.

We propose a generalized approach to include the actual concentration of cations $[A^+]$ and anions $[X^-]$ not only due to the pH-values but also the presence of additional solvents, where they change the ionic density but not the pH-value of the electrolyte. Therefore, a common approach from chemistry is adopted. The molar ionic strength is a measure of the concentration of the active ions, as a function of all ions present in the solution ($I = 1/2 \sum c_i z_i^2$) [24], [25]. Usually this parameter is used to calculate the molar conductivity where z_i is the charge number (valency), and c_i the concentration. Here, it is similarly used to find an average value for the positive and negative charge (cations and anions) carriers.

$$\begin{cases} c_A^+ = [A^+] = \alpha |zA| \cdot c_{01} A_b \\ c_X^- = [X^-] = \alpha |zX| \cdot c_{02} X_b \end{cases} \quad (2)$$

The individual concentrations are first expressed by a parameter α , the charge number z , and the initial concentration c_{0i} , which are then added up to a total concentration. The parameter α reflects a value based on the degree of dissociation depending on the electrolyte and the activity coefficient of the ionic liquids which changes with different electrolytes. For a 1:1 electrolyte the $zA = +1$ is the cation charge, $zX = -1$ is the anion charge, cA_b is the electrolyte A^+ concentration and cX_b is the electrolyte X^- concentration.

Solving equation (1) for ion activity and adding up with equation (2) gives the actual number of charged particles

$$\begin{cases} c_{0,tot}^+ = [A^+] + [H^+] = \alpha |zA| \cdot cA_b + 10^{-pH} \\ c_{0,tot}^- = [X^-] + [OH^-] = \alpha |zX| \cdot cX_b + 10^{-(14-pH)} \end{cases} \quad (3)$$

With the Avogadro constant $N_{av} = 6.02 \cdot 10^{23} \text{ mol}^{-1}$ and the factor of $1L = 1000 \text{ cm}^3$, all positive and negative charges

can be expressed in $[\text{ions}] / \text{cm}^3$

$$\begin{cases} p = c_{0,tot}^+ \cdot N_{av} \frac{1}{\text{mol}} \cdot 10^{-3} \frac{\text{L}}{\text{cm}^3} \\ n = c_{0,tot}^- \cdot N_{av} \frac{1}{\text{mol}} \cdot 10^{-3} \frac{\text{L}}{\text{cm}^3} \end{cases} \quad (4)$$

With the general validity of the electroneutrality conditions, the equilibrium charge can be captured on the scope of classic semiconductor physics.

The distinctive feature of the electrolyte at its interface to the channel is due to the applied bias which arranges the ions according to the theory of Gouy-Chapman and Helmholtz [21], in a Stern-layer and a diffusion layer [26].

In the basic sense, the charge carrier profile of such an interface can be represented by the Poisson-Boltzmann equation [23], [27], [28]. However, this approximation neglects the real ionic size and the subdivision into the mentioned layers.

$$\frac{\partial^2 \phi}{\partial x^2} = \frac{-q}{\epsilon} \left[c_0^+ \exp\left(\frac{-q\phi(x)}{k_B T}\right) - c_0^- \exp\left(\frac{q\phi(x)}{k_B T}\right) \right] \quad (5)$$

This ordinary non-linear second order differential equation determines the electrostatic potential ϕ along the solution. The x denotes the distance away from the interface, c_0^+ and c_0^- are the cation and anion concentrations, $\epsilon = \epsilon_0 \cdot \epsilon_r$ is the permittivity of water, T is the lattice temperature and k_B is the Boltzmann factor.

B. SIMULATION METHOD

The adapted material to represent the electrolyte is implemented in the Synopsys Sentaurus TCAD software [29] to enable TCAD simulation of OECTs. Where the new material must accomplish the physics, initial properties, and the key characteristics like expected surface charge and potential in an electrolyte. This can be done by modeling the electrolyte as an intrinsic semiconductor and using the Fermi-Dirac statistics. In fact, the Fermi-Poisson equation is identical to equation (5) when the Density of States (DOS) and the bandgap E_G of the intrinsic semiconductor are chosen properly [28], [30].

For an intrinsic semiconductor, the relation of energy differences from valence band, conduction band and quasi-Fermi level can be simplified with the estimation that the energy difference is about half of the bandgap: $E_c - E_i = E_i - E_v = E_G/2$. Therefore, the electrolyte hole “cation” and electron “anion” density can be therefore stated as [23]

$$\begin{cases} p = N_V \exp\left(\frac{-E_G}{2k_B T}\right) \\ n = N_C \exp\left(\frac{-E_G}{2k_B T}\right) \end{cases} \quad (6)$$

where N_V and N_C are the effective DOS for holes and electrons in the valence and conduction bands, respectively.

Since it is not possible for Sentaurus to distinguish between ions and electrons, one has to set a fixed DOS so that the density of charge carries corresponds to its counterpart, i.e., $p \propto c_{0,tot}^+$ and $n \propto c_{0,tot}^-$ (see equation (4)) which is expected to describe the experimental situation in

OECTs realistically. By substituting expression (4) into (6) and rewrite it respectively to the DOS results in

$$\begin{cases} N_V = [\alpha|zA|\cdot cA_b + 10^{-pH}] \exp\left(\frac{E_G}{2k_B T}\right) N_{av} 10^{-3} \\ N_C = [\alpha|zX|\cdot cX_b + 10^{-(14-pH)}] \exp\left(\frac{E_G}{2k_B T}\right) N_{av} 10^{-3} \end{cases} \quad (7)$$

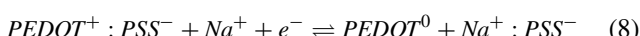
For instance for a 3mol/L electrolyte with $Z = 1$, $\alpha = 0.001$ and a pH -value of 7, with an arbitrary bandgap of 1.5eV , the required DOS can be determined as 10^{30} .

Fig. 2 shows the simulated OECT with the proposed electrolyte at the applied biases of $V_{DS} = -0.5\text{V}$ and $V_{GS} = (+1, 0, -1)\text{V}$. The cation distribution and concentration in the electrolyte based on the proposed method is shown in Fig. 2(a). Depending on the expected cation density in an electrolyte for instance $1\text{e}16 \text{ cm}^{-3}$, one needs to consider a hole DOS $N_V = 5\text{e}28 \text{ cm}^{-3}$ according to equation (6). Since the electrical double layer capacitance is almost independent of the electrolyte thickness, we have shown the simulation results for an electrolyte thickness of 300nm . The cation and anion distribution and concentration in the electrolyte with the applied gate and drain biases are shown in Fig. 2(b) and Fig. 2(c) based on equation (5). The position refers to the cross-section through the electrolyte (see the dash arrow in Fig. 2(a)), where 0nm indicates the electrolyte-gate interface and 300nm means electrolyte-channel interface.

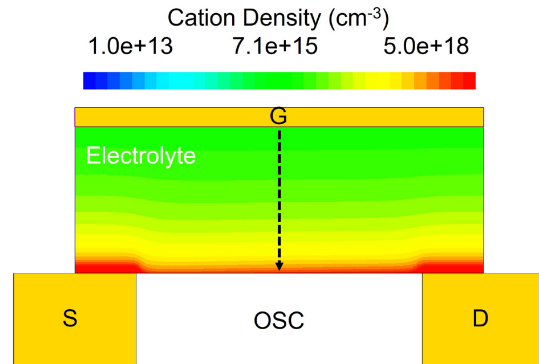
Please note that the oxide layer is only present on the channel side thus prevents a charge transfer between electrolyte and the channel region. Thereby, an EDL will form at electrolyte-semiconductor interface according to equation (5) and the charge density given by equation (4). However, there is no oxide layer on the gate side because of simplification, thus the charges can be injected or extracted at the gate side (similar to an electrolyte-gated transistor). In fact, the position $x = 0\text{nm}$ does not represent the electrical double layer at the gate side and has no influence on the device behavior, but rather an extension of the bulk of the electrolyte in which the equilibrium concentration is present. By applying a V_{GS} , the propagation of potential/field strength into the OSC-channel region determines the surface potential and dictate device performance.

C. ORGANIC SEMICONDUCTOR

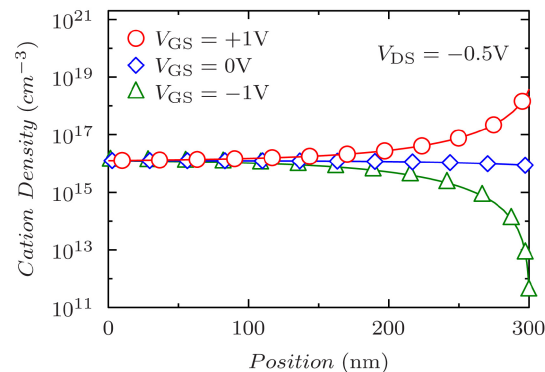
Doping and de-doping are the underlying chemical mechanism that enhance the OMIECs/OECTs performance [31]. Charging mechanism is given by the redox reaction [16]:



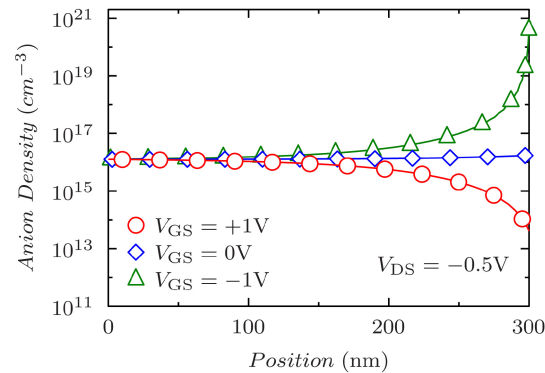
We have considered incomplete ionization with an ionization probability model based on activation energy to emulate doping and de-doping in the OMIEC. The initial hole concentration is proportional to the redox reaction of the oxidized polymer chain. In its doped state, the PEDOT hole density corresponds roughly to a value of 10^{18} to 10^{21} per cm^3 [32]. Since this is directly proportional to the number of mobile holes, then an acceptor-dopant is used to replace them. Similar to the Fermi-Dirac distribution, the



(a) Cation density at $V_{DS} = -0.5\text{V}$ and $V_{GS} = +1\text{V}$



(b) Cation distribution and concentration



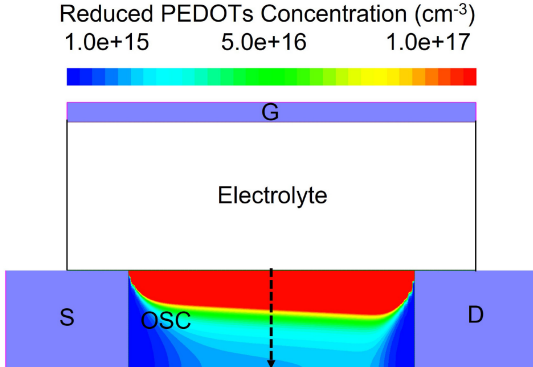
(c) Anion distribution and concentration

FIGURE 2. (a) OECT structure showing the simulated cation density of $1\text{e}16 \text{ cm}^{-3}$ in the proposed electrolyte with $N_V = 5\text{e}28 \text{ cm}^{-3}$ at $V_{DS} = -0.5\text{V}$ and $V_{GS} = +1\text{V}$ (b) cation and (c) anion distribution and concentrations in the electrolyte through the shown dash arrow at $V_{DS} = -0.5\text{V}$ and $V_{GS} = (+1, 0, -1)\text{V}$.

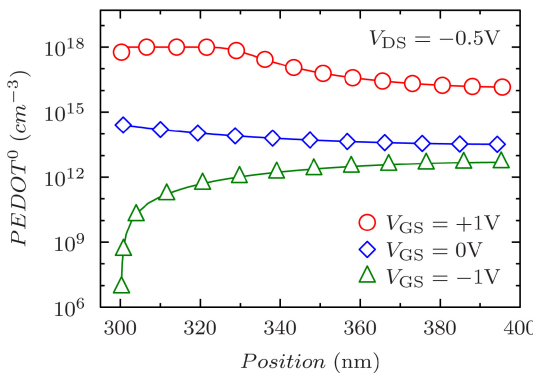
ionic concentration follows an exponential law [29] and is given by

$$N_A = \frac{N_{A,0}}{1 + g_A \cdot \exp\left(\frac{E_A - E_{F,p}}{k_B T}\right)} \quad (9)$$

where $N_{A,0}$ is the substitutional (active) acceptor concentration, g_A is the degeneracy factor for the doping level. The



(a) Reduced PEDOT ($PEDOT^0$) concentration at $V_{DS} = -0.5V$ and $V_{GS} = +1V$



(b) Density of reduced PEDOT ($PEDOT^0$) in OMIEC

FIGURE 3. Simulated OECT structure showing the ionized acceptor concentration at $V_{DS} = -0.5V$ and $V_{GS} = +1V$ and (b) bias dependent density of reduced PEDOTs through the OSC-thickness indicated with dash arrow at $V_{DS} = -0.5V$ and $V_{GS} = (+1, 0, -1)V$.

parameter E_A is the acceptor ionization (activation) energy, and $E_{F,p}$ is the quasi-Fermi energy for holes.

The Fig. 3 shows the simulated OECT with incomplete ionization as mentioned in equation (9). The reduced PEDOT ($PEDOT^0$) concentration in the OMIEC is shown at $V_{DS} = -0.5V$ and $V_{GS} = +1V$ in Fig. 3(a). The bias dependent reduced PEDOT is depicted (see Fig. 3(b)) at $V_{DS} = -0.5V$ and $V_{GS} = (+1, 0, -1)V$. The position refers to the cross-section through the OSC thickness (see the dash arrow in Fig. 3(a)), where 300 nm indicates the electrolyte-OMIEC interface. A bias dependent incomplete ionization resembles doping and de-doping behavior and more accurate parameter values can be extracted based on the actual experimental performance and additional characterization of the fabricated devices.

A Gaussian DOS has been considered for disordered OMIECs with

$$g(E) = \frac{N_t}{\sqrt{2\pi}\sigma_{DOS}} \exp\left(-\frac{(E - E_c)^2}{2\sigma_{DOS}^2}\right), \quad (10)$$

where N_t is the total number of hopping sites with $N_t = N_{LUMO}$ for electrons and $N_t = N_{HOMO}$ for holes, σ_{DOS} is

TABLE 2. Parameters.

| Parameter | Description | Value |
|---------------------|----------------------------------|-------------------------|
| cH_b | Electrolyte H^+ concentration | $10^{-7} mol L^{-1}$ |
| cOH_b | Electrolyte OH^- concentration | $10^{-7} mol L^{-1}$ |
| cA_b | Electrolyte A^+ concentration | $3 mol L^{-1}$ |
| cX_b | Electrolyte X^- concentration | $3 mol L^{-1}$ |
| α | activity coefficient | 0.001 |
| zA | Cation charge | +1 |
| zX | Anion charge | -1 |
| pH | pH-value | 7 |
| N_C, N_V | DOS Electrolyte | $\sim 10^{30} cm^{-3}$ |
| ϵ_r | Relative permittivity of water | 78.5 |
| χ_E | Electrolyte e-affinity | 4.3eV |
| E_G | Electrolyte Bandgap | 1.5eV |
| $\mu_{0,elec}$ | Ion Mobility | $10^{-3} cm^2(Vs)^{-1}$ |
| χ_{OMIEC} | OMIEC e-affinity | 1.8eV |
| $E_G, OMIEC$ | OMIEC Bandgap | 3.3eV |
| $\mu_{0,OMIEC}$ | constant mobility | $4 cm^2(Vs)^{-1}$ |
| $\epsilon_r, OMIEC$ | Relative permittivity OMIEC | 12 |
| β | Poole-Frenkel coefficient | 1 |
| γ | Poole-Frenkel coefficient | 0 |
| E_0 | Effective activation energy | -0.15eV |
| $N_{A,0}$ | OMIEC p-Doping density | $10^{18} cm^{-3}$ |
| E_A | Ionization activation energy | 0.65eV |
| g_A | Degeneracy factor | 4 |
| N_t | Number of hopping sites | $10^{21} cm^{-3}$ |
| σ_{DOS} | Width of the Gaussian DOS | 0.081eV |
| E_c | Energy center | 0.1eV |
| $W_{F(S/D/G)}$ | Source/Drain/Gate workfunction | 4.85eV |
| T | Temperature | 300K |

the width of the Gaussian DOS distribution, and E_c is the energy center.

A Gaussian DOS and drift-diffusion has been used together with a Poole-Frenkel mobility model with a square-root dependence on the electric field expressed as

$$\mu(F) = \mu_0 \exp\left(-\frac{E_0}{k_B T}\right) \exp\left(\sqrt{F}\left(\frac{\beta}{T} - \gamma\right)\right), \quad (11)$$

where μ_0 is the low-field mobility, E_0 is the effective activation energy, β and γ are Poole-Frenkel coefficient and F is the applied electric field.

Schottky contacts are considered at source and drain interface with the OMIEC. Therefore, the injection barrier is determined by the work function of the channel and electrode materials. The saturation current in the experimental transfer characteristics of OECT can be attributed to saturated injection from the source, and the used parameters in the simulation are given in Table 2.

IV. MODEL RESULTS AND VERIFICATION

The experimental data of fabricated OECTs have been used to validate the developed method and models. The above-mentioned numerical model has been used to simulate the behavior of OECTs with various bias conditions. Table 1 shows the geometric parameters and Table 2 shows the material parameters that are used for the TCAD simulation and numerical model of OECTs.

Fig. 4 shows the forward-backward sweep transfer measurements (symbols) of a fabricated OECT with $W_{Ch} = 150\mu m$, and $L_{Ch} = 50\mu m$ compared to the simulation

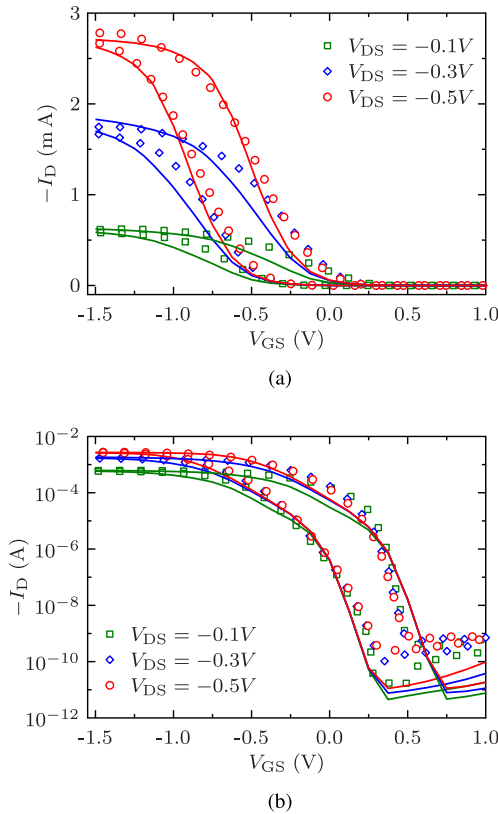


FIGURE 4. Experimental data (symbols) and numerical TCAD simulation results (solid lines) for a single gate OECT in both (a) linear and (b) logarithmic scales at $V_{DS} = (-0.1, -0.3, -0.5)V$.

(solid lines) results at $V_{DS} = (-0.1, -0.3, -0.5)V$. The developed numerical model shows a good agreement compared to the actual measurements in both linear (Fig. 4(a)) and logarithmic (Fig. 4(b)) scales. The output characteristics based on the numerical model (solid line) compared to measured data (symbols) are depicted in Fig. 5 at $V_{GS} = (0.25, 0, -0.25, -0.5)V$.

Although there are some discrepancies between measured data in comparison to the numerical model, however, the overall behavior is well captured. Trap characterization [33] of the fabricated OECTs might be needed to incorporate a proper contribution of traps to further increase the accuracy of numerical modeling of such devices. Furthermore, a detailed investigation on the transient properties needs to be performed in order to fully capture and analyze the dynamic properties of the OECTs.

Please note that the implemented model and the use of an additional oxide layer in the channel side [see Fig. 1(b)] primarily capture the electrostatic behavior and properties of the electrolyte-channel interface. This means the formation of EDL based on electrolyte with mobile ions and its influence on the performance of OECTs is captured properly and simulated correctly. The incomplete ionization model incorporates a possible ionic injection into the OMIEC layer and the associated effects are included in the developed model. The developed method and incomplete ionization model can be

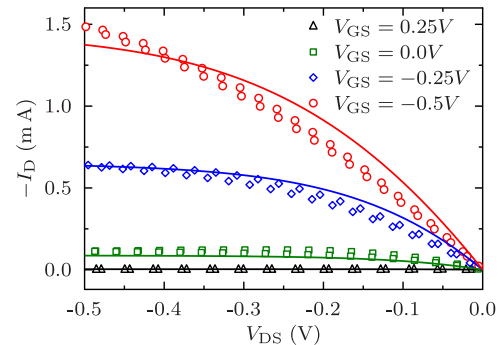


FIGURE 5. Output characteristics of the single gate OECT obtained from numerical TCAD simulation (solid lines) compared to the measured data (symbols) at $V_{GS} = (0.25, 0, -0.25, -0.5)V$.

adapted to other organic semiconductors with properly incorporating the considered organic semiconductor parameters and associated redox reaction properties.

In fact, one of the main reasons for the high drain current in OECTs is due to the high cation density over the small distance of the Helmholtz plane (see Fig. 2(b)). The exact size is depending on the Debye length and the density of ions. All together, an electric field in the order of $\sim 10^6$ V/cm is achieved which matches well the ones stated in the literature [34], [35]. This leads to a very large capacitance (different from the conventional capacitance and negligible influence of the electrolyte thickness) resulting in a low voltage operating device with a high transconductance. The saturation in the transfer characteristics can also possibly be attributed to a screening by the Helmholtz plane leading to the pinned surface potential (independent of additional increase of the V_{GS}). Despite the simplicity of the approach, the behavior of OECTs is well-captured by the proposed new formulations and shows good agreement with the experimental data.

V. CONCLUSION

A numerical formulation for the ion distribution and movement in the electrolyte materials and incomplete ionization model in OMIEC layer has been derived for modeling of the OECT performance. A proper implementation of an electrolyte as a key element for the OECTs performance defined through an effective method using an intrinsic semiconductor which enables to model EDL behavior. The incomplete ionization for selected species has been proposed with an ionization probability model based on activation energy. This has enabled to mimic doping and de-doping in the OMIEC layer of OECTs with the applied biases. The comparison with experimental data of fabricated OECTs shows a good agreement with the proposed formulation. The presented models enable numerical simulation, analysis, design, optimization and to investigate the operation mechanism and behavior of OECTs as a proper building block for synaptic devices and functionality.

REFERENCES

- [1] B. Zhou, W. Liu, Y. Xu, C. Jin, J. Yang, and J. Sun, "Organic electrochemical transistors toward synaptic electronics," *J. Phys. D, Appl. Phys.*, vol. 55, no. 30, May 2022, Art. no. 304006. [Online]. Available: <https://dx.doi.org/10.1088/1361-6463/ac67b9>
- [2] P. C. Harikesh et al., "Organic electrochemical neurons and synapses with ion mediated spiking," *Nat. Commun.*, vol. 13, no. 1, p. 901, Feb. 2022. [Online]. Available: <https://doi.org/10.1038/s41467-022-28483-6>
- [3] S. Sinha and T. Pal, "A comprehensive review of FET-based pH sensors: Materials, fabrication technologies, and modeling," *Electrochem. Sci. Adv.*, vol. 2, no. 5, Oct. 2021, Art. no. e2100147. [Online]. Available: <https://doi.org/10.1002/elsa.202100147>
- [4] X. Ji et al., "Mimicking associative learning using an ion-trapping non-volatile synaptic organic electrochemical transistor," *Nat. Commun.*, vol. 12, no. 1, p. 2480, 2021. [Online]. Available: <https://doi.org/10.1038/s41467-021-22680-5>
- [5] P. Gkoupidenis, N. Schaefer, X. Strakosas, J. A. Fairfield, and G. G. Malliaras, "Synaptic plasticity functions in an organic electrochemical transistor," vol. 107, no. 26, Dec. 2015, Art. no. 263302. [Online]. Available: <https://doi.org/10.1063/1.4938553>
- [6] J. Rivnay, S. Inal, A. Salleo, R. M. Owens, M. Berggren, and G. G. Malliaras, "Organic electrochemical transistors," *Nat. Rev. Mater.*, vol. 3, no. 2, Jan. 2018, Art. no. 17086. [Online]. Available: <https://doi.org/10.1038/natrevmats.2017.86>
- [7] B. D. Paulsen, K. Tybrandt, E. Stavrinidou, and J. Rivnay, "Organic mixed ionic-electronic conductors," *Nat. Mater.*, vol. 19, no. 1, pp. 13–26, Aug. 2019. [Online]. Available: <https://doi.org/10.1038/s41563-019-0435-z>
- [8] H. Ling, D. A. Koutsouras, S. Kazemzadeh, Y. van de Burgt, F. Yan, and P. Gkoupidenis, "Electrolyte-gated transistors for synaptic electronics, neuromorphic computing, and adaptable biointerfacing," *Appl. Phys. Reviews*, vol. 7, no. 1, Mar. 2020, Art. no. 11307. [Online]. Available: <https://doi.org/10.1063/1.5122249>
- [9] A. Weissbach, L. M. Bongartz, M. Cucchi, H. Tseng, K. Leo, and H. Kleemann, "Photopatternable solid electrolyte for integrable organic electrochemical transistors: Operation and hysteresis," *J. Mater. Chem. C*, vol. 10, no. 7, pp. 2656–2662, 2022. [Online]. Available: <https://doi.org/10.1039/DITC04230K>
- [10] C. Liao, M. Zhang, M. Y. Yao, T. Hua, L. Li, and F. Yan, "Flexible organic electronics in biology: Materials and devices," *Adv. Mater.*, vol. 27, no. 46, pp. 7493–7527, Nov. 2014. [Online]. Available: <https://doi.org/10.1002/adma.201402625>
- [11] I. Gualandi, M. Marzocchi, A. Achilli, D. Cavedale, A. Bonfiglio, and B. Fraboni, "Textile organic electrochemical transistors as a platform for wearable biosensors," *Sci. Rep.*, vol. 6, no. 1, 2016, Art. no. 33637. [Online]. Available: <https://doi.org/10.1038/srep33637>
- [12] D. Khodagholy et al., "Organic electrochemical transistor incorporating an ionogel as a solid state electrolyte for lactate sensing," *J. Mater. Chem.*, vol. 22, no. 10, p. 4440, 2012. [Online]. Available: <https://doi.org/10.1039/C2JM15716K>
- [13] C. P. H. Rajapaksha et al., "Ionic liquid crystal elastomers-based flexible organic electrochemical transistors: Effect of director alignment of the solid electrolyte," *Appl. Phys. Rev.*, vol. 9, no. 1, Mar. 2022, Art. no. 11415. [Online]. Available: <https://doi.org/10.1063/5.0077027>
- [14] H. Tseng et al., "Threshold voltage control in dual-gate organic electrochemical transistors," *Adv. Mater. Interfaces*, to be published. [Online]. Available: <https://doi.org/10.1002/admi.202201914>
- [15] S. H. Kim et al., "Electrolyte-gated transistors for organic and printed electronics," *Adv. Mater.*, vol. 25, no. 13, pp. 1822–1846, Dec. 2012. [Online]. Available: <https://doi.org/10.1002/adma.201202790>
- [16] M. Cucchi et al., "Thermodynamics of organic electrochemical transistors," *Nat. Commun.*, vol. 13, no. 1, p. 4514, Aug. 2022. [Online]. Available: <https://doi.org/10.1038/s41467-022-32182-7>
- [17] M. Koch et al., "Numerical modeling of organic electrochemical transistors," in *Proc. IEEE Latin Amer. Electron Devices Conf. (LAEDC)*, Jul. 2022, pp. 1–14. [Online]. Available: <https://ieeexplore.ieee.org/document/9908245>
- [18] H. Kleemann, A. Zakhidov, M. Anderson, T. Menke, K. Leo, and B. Luessem, "Direct structuring of C60 thin film transistors by photo-lithography under ambient conditions," *Org. Electron.*, vol. 13, no. 3, pp. 506–513, Mar. 2012. [Online]. Available: <https://doi.org/10.1016/j.orgel.2011.12.009>
- [19] M. Hoeppner, D. Kneipe, H. Kleemann, and K. Leo, "Precise patterning of organic semiconductors by reactive ion etching," *Org. Electron.*, vol. 76, Jan. 2020, Art. no. 105357. [Online]. Available: <https://doi.org/10.1016/j.orgel.2019.07.015>
- [20] H. Du, X. Lin, Z. Xu, and D. Chu, "Electric double-layer transistors: A review of recent progress," *J. Mater. Sci.*, vol. 50, no. 17, pp. 5641–5673, 2015. [Online]. Available: <https://doi.org/10.1007/s10853-015-9121-y>
- [21] H. Helmholtz, "Ueber einige Gesetze der Vertheilung elektrischer Ströme in körperlichen Leitern, mit Anwendung auf die thierisch-elektrischen Versuche (Schluss)," *Annalen der Physik und Chemie*, vol. 165, no. 7, pp. 353–377, 1853. [Online]. Available: <https://doi.org/10.1002/andp.18531650702>
- [22] J. Bisquert, *The Physics of Solar Energy Conversion*. Boca Raton, FL, USA: CRC Press, Jun. 2020. [Online]. Available: <https://doi.org/10.1201/9780429505874>
- [23] D. Passeri, A. Morozzi, K. Kanxheri, and A. Scorzoni, "Numerical simulation of ISFET structures for biosensing devices with TCAD tools," *BioMed. Eng. OnLine*, vol. 14, no. S2, p. S3, 2015. [Online]. Available: <https://doi.org/10.1186/1475-925X-14-S2-S3>
- [24] M. Schrader, *Prinzipien und Anwendungen der Physikalischen Chemie*. Heidelberg, Germany: Springer, 2016. [Online]. Available: <https://link.springer.com/book/10.1007/978-3-642-41730-6>
- [25] J. Blahous, *Uebungen zur Physikalischen Chemie*. Vienna, Austria: Springer, 2001. [Online]. Available: <https://link.springer.com/book/10.1007/978-3-7091-6749-6>
- [26] R. R. Job, *Physikalische Chemie*. Berlin, Germany: Springer-Verlag GmbH, Feb. 2021. [Online]. Available: https://www.ebook.de/de/product/40325615/georg_job_regina_rueffler_physikalische_chemie.html
- [27] I.-Y. Chung, H. Jang, J. Lee, H. Moon, S. M. Seo, and D. H. Kim, "Simulation study on discrete charge effects of SiNW biosensors according to bound target position using a 3D TCAD simulator," *Nanotechnology*, vol. 23, no. 6, Jan. 2012, Art. no. 65202. [Online]. Available: <https://dx.doi.org/10.1088/0957-4484/23/6/065202>
- [28] E. Mohammadi and N. Manavizadeh, "An accurate TCAD-based model for ISFET simulation," *IEEE Trans. Electron Devices*, vol. 65, no. 9, pp. 3950–3956, Sep. 2018. [Online]. Available: <https://ieeexplore.ieee.org/document/8423497>
- [29] *Sentaurus Device User Manual*, Synopsys, Synopsys, Mountain View, CA, USA, 2022.
- [30] R. Narang, M. Saxena, and M. Gupta, "Analytical model of pH sensing characteristics of junctionless silicon on insulator ISFET," *IEEE Trans. Electron Devices*, vol. 64, no. 4, pp. 1742–1750, Apr. 2017. [Online]. Available: <https://ieeexplore.ieee.org/document/7865909>
- [31] S. T. Keene et al., "Enhancement-mode PEDOT:PSS organic electrochemical transistors using molecular de-doping," *Adv. Mater.*, vol. 32, no. 19, Mar. 2020, Art. no. 2000270. [Online]. Available: <https://doi.org/10.1002/adma.202000270>
- [32] A. Shirinskaya, G. Horowitz, J. Rivnay, G. Malliaras, and Y. Bonnassieux, "Numerical modeling of an organic electrochemical transistor," *Biosensors*, vol. 8, no. 4, p. 103, Oct. 2018. [Online]. Available: <https://doi.org/10.3390/bios8040103>
- [33] G. Darbandy et al., "Characterization of the charge-trap dynamics in organic thin-film transistors," in *Proc. 26th Int. Conf. Mixed Design Integr. Circuits Syst.*, 2019, pp. 76–80. [Online]. Available: <https://ieeexplore.ieee.org/document/8787105>
- [34] T. Fujimoto and K. Awaga, "Electric-double-layer field-effect transistors with ionic liquids," *Phys. Chem. Chem. Phys.*, vol. 15, no. 23, p. 8983, 2013. [Online]. Available: <https://doi.org/10.1039/C3CP50755F>
- [35] N. Liu, R. Chen, and Q. Wan, "Recent advances in electric-double-layer transistors for bio-chemical sensing applications," *Sensors*, vol. 19, no. 15, p. 3425, Aug. 2019. [Online]. Available: <https://doi.org/10.3390/s19153425>